Integrating LiDAR-Derived Terrain Models and GIS Analysis for Flood Risk Assessment: A Case Study in the Argeșel Basin, Romania

Ioana VIZIREANU, Dan RĂDUCANU, Liviu PORUMB and Lucian Marius NECULA

***Abstract*—Flood risk assessment needs detailed topography to recover realistic flow paths and identify vulnerable assets. This study targets the Argesel Basin in southern Romania, a small flood-prone catchment with fast runoff response. High-density airborne LiDAR was processed into a 1 m Digital Terrain Model (DTM) and hydrologically conditioned (culvert continuity, breakline enforcement, removal of artefacts) to restore drainage connectivity. On this surface, slope and flow accumulation were derived, depressions (“bluespots”) were mapped, and storage–elevation curves with pour-point thresholds supported a fill–spill hierarchy. A rainfall-to-fill screening (mm = V/Ac) provided site-specific spill thresholds, which were intersected with building footprints for exposure metrics. Results show pronounced susceptibility: 72 of 75 depressions (about 96%) would reach spill at or below 30 mm of effective rainfall, and roughly 83% lie at or below 10 mm; the maximum threshold is ~56 mm. Susceptibility concentrates along the Argesel floodplain and near the Valea lui Topor and Mazgana confluences, highlighting priority locations where culvert performance likely governs outcomes. The contribution is a reproducible GIS workflow that couples a culvert-enforced 1 m DTM with a fill–spill hierarchy and rainfall-to-fill thresholds to deliver actionable, site-level screening for local planning in small basins.**

***Index Terms*—Airborne LiDAR, Digital Terrain Model, Flood Risk, GIS Analysis, Hydrological Simulation.**

I. Introduction

Reliable local-scale flood risk assessment hinges on the quality of terrain information used to derive flow paths, storage, and connectivity. High-resolution processing of digital elevation models (DEMs) has advanced markedly with efficient depression-handling algorithms such as Priority-Flood, improving both accuracy and speed for hydrologic preprocessing [1]. For screening and planning, geometric, network-based approaches like Arc-Malstrøm identify depressions (“bluespots”), delineate contributing areas, and route potential overflow between storage units, providing an interpretable, first-order picture of pluvial susceptibility [2].

In practical flood mapping workflows, high-density airborne LiDAR is first leveraged to produce Digital Terrain Models (DTMs) at sub-meter to meter resolution, preserving micro-topographic features—breaklines, small channels, road embankments, and culverts—that strongly influence overland routing and local storage. These surfaces should then be hydro-conditioned so that drainage connectivity is restored and artificial artefacts are removed prior to any inundation screening or modelling [3, 4].

Beyond channel hydraulics, terrain-derived indices are subsequently computed to characterize susceptibility patterns. In particular, slope, flow accumulation, and variants of wetness or sink-depth metrics have proven informative; a synthesis in urban settings shows these indices capture hotspots of waterlogging when derived from high-resolution, hydro-conditioned DEMs [5]. A broader review confirms that LiDAR-derived DEMs generally outperform coarser products for flood applications, provided artefacts are removed and connectivity is enforced prior to analysis [3].

Evidence from Romania underscores the benefit of this sequence. In the Jijia floodplain, 1D HEC-RAS modelling on 0.5 m LiDAR DEMs produced more realistic flood extents and exposure than official products built on lower-resolution terrain, underscoring the value of high-fidelity topography for risk mapping [6]. Complementary work in north-eastern basins reached similar conclusions, emphasizing that hydro-enforced LiDAR DEMs are pivotal for precise floodplain characterization [7].

Algorithmic choices then govern operational efficiency. Recent variants of Priority-Flood reduce compute time on large rasters while retaining hydrologic fidelity, enabling faster end-to-end workflows where multiple scenarios must be screened [8]. Where anthropogenic embankments or linear infrastructure obstruct realistic drainage, breaching–filling hybrids minimize distortion of flow paths compared to pure pit-filling, preserving the micro-channel network that controls overland routing [4].

Uncertainty associated with DEM source, resolution, and conditioning propagates into hydrologic derivatives and, ultimately, hazard delineation. Field-scale analyses demonstrate that changing grid size and sink-removal strategy alters divides, flow lengths, and accumulation patterns, with implications for exposure mapping if left unaccounted [9]. Fluvial inundation studies similarly quantify systematic biases stemming from degraded DEM resolution and vertical error, reinforcing the case for LiDAR-grade inputs or careful downscaling strategies in data-sparse contexts [10].

At broader scales, model–data comparisons show that global DEMs (e.g., SRTM-family) frequently over- or

I. VIZIREANU is with the Military Technical Academy “Ferdinand I”, and the INCAS - National Institute for Aerospace Research “Elie Carafoli”, Bucharest, Romania (e-mail: vizireanu.ioana@incas.ro).

D. RĂDUCANU is with the Military Technical Academy “Ferdinand I”, Bucharest, Romania (e-mail: dan.raducanu@gmail.com).

L. PORUMB is with the Military Technical Academy “Ferdinand I”, Bucharest, Romania (e-mail: porumb_liviu@yahoo.com).

L.M. NECULA is with the Military Technical Academy “Ferdinand I”, Bucharest, Romania (e-mail: marius.lucian.necula@gmail.com).

Digital Object Identifier 10.32754/JMT.2026.1.19

underestimate inundation relative to LiDAR benchmarks—particularly in built environments—affecting both flood extents and impact estimates; higher-quality elevations substantially reduce such biases [11]. When high-resolution topography is unavailable, ensemble and simulation-based approaches can partially compensate, yet performance still hinges on DEM realism and artefact suppression [12].

Methodologically, explicit coupling between depression storage and overflow thresholds provides transparent scenario analysis at fine scales. The Fill–Spill–Merge paradigm and related flow-tracing developments connect nested depression hierarchies and enable computation of storage filling and spill sequences, aligning well with bluespot screening for pluvial scenarios [13]. For national- to continental-scale assessments, combined fluvial, pluvial, and coastal hazard modelling at ~tens-of-meters resolution has become feasible; nevertheless, local planning continues to benefit most from high-resolution, hydro-enforced terrain workflows [14].

A LiDAR-based, GIS-centric workflow is developed for the Argeșel Basin (southern Romania). The sequence comprises of: the generation of a 1 m hydro-enforced DTM; derivation of slope and accumulation layers; the application of Arc-Malstrøm bluespot screening; and the exposure analysis for buildings. This approach is conceptually compatible with depression-handling and breaching best practices and is intended for rapid, reproducible screening that complements detailed hydraulic modelling where inputs permit [15].

II. Study Area and Data Description

A. Study Area

The study area lies in Argeș County (southern Romania) and includes the localities of Hârtiești, Dealu, and Vulturești, covering 15 km² within the Argeșel River basin. The Argeșel flows north–south across the area, while its semi-permanent to ephemeral tributaries, Valea lui Topor and Mâzgana, activate mainly during wet spells and govern local flood exposure in low-lying sectors. The terrain belongs to the Getic Piedmont, where gully-prone slopes and relief dissection enhance runoff concentration toward valley bottoms [16]. Fig. 1 shows the study-area boundary, river network, and settlements.

The regional hydroclimate is colline, with rainfall maxima typically in May–June. Recurrent flood episodes have been documented in adjacent basins of Argeș County and the Argeș–Vedea region, including process-based reconstructions of a major event on the Vedea River and basin-scale applications in the Argeș system, which support the need for high-resolution, local-scale risk assessment in nearby small catchments [17, 18].

B. LiDAR Data

Airborne topographic LiDAR was acquired using a fixed-wing survey platform (Hawker Beechcraft King Air C90 GTx) carrying a RIEGL LMS-Q680i full-waveform, near-infrared airborne laser scanner. Flight planning targeted uniform coverage with 35% side overlap between adjacent flight lines. Acquisition altitude was 550 m above ground level (AGL) and ground speed 70 m s^{-1}, producing a mean point density of 8 points m^{-2} over 15 km². The instrument supports multiple returns and full-waveform recording, with typical operating capabilities including up to 400 kHz laser pulse repetition rate and a 60° field of view, suitable for floodplain and small-catchment mapping [19]. Delivered inputs consisted of raw point clouds in LAS/LAZ with per-return intensity and trajectory metadata, which served as the sole elevation source for subsequent terrain modelling and GIS analyses.

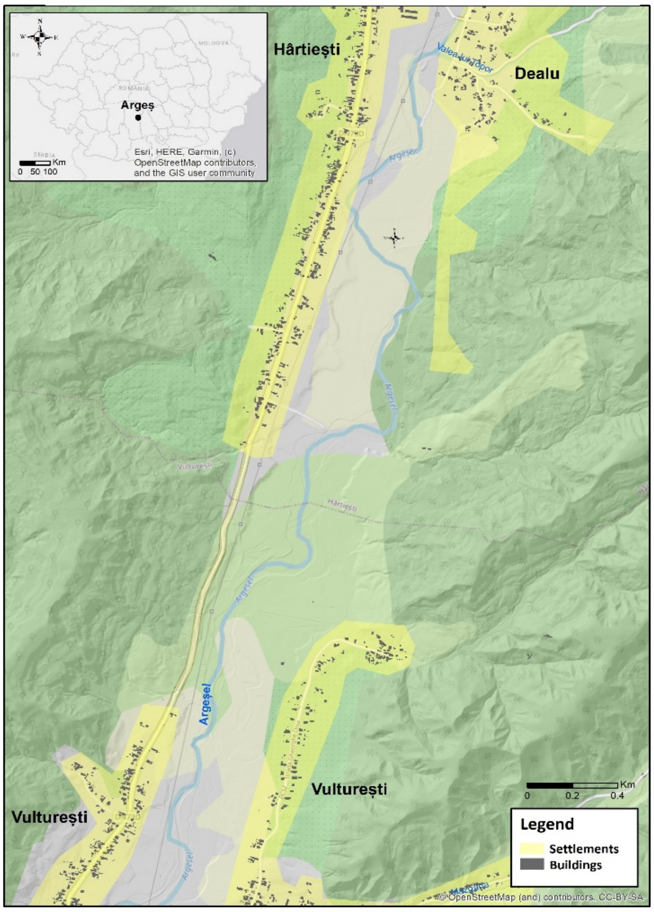

Figure 1. Study area map

III. Methodology

Processing relied on a 1 m LiDAR-derived Digital Terrain Model that was hydrologically conditioned to preserve drainage connectivity across culverts and road embankments and to remove residual artefacts before any routing or storage analysis [20]. On the conditioned surface, flow direction/accumulation were derived, closed depressions ("bluespots") were mapped in ArcGIS Desktop, and these were organised into a fill–spill hierarchy with storage–elevation relations and pour-point thresholds. Pluvial screening used uniform rainfall depths expressed as rainfall depth to fill $(\mathrm{mm} = V/A_c)$, and a local drainage-capacity threshold of 30 mm h^{-1} was adopted to flag depressions likely to spill under design rainfall. The resulting composite depression footprints at spill onset were intersected with building footprints to obtain exposure metrics (number of affected buildings, impacted area, depth). For communication purposes, water-level visualisations at +1 m and +2 m were

 Digital Object Identifier 10.32754/JMT.2026.1.19

produced in Global Mapper/ArcScene. The overall sequence is summarised in Fig. 2.

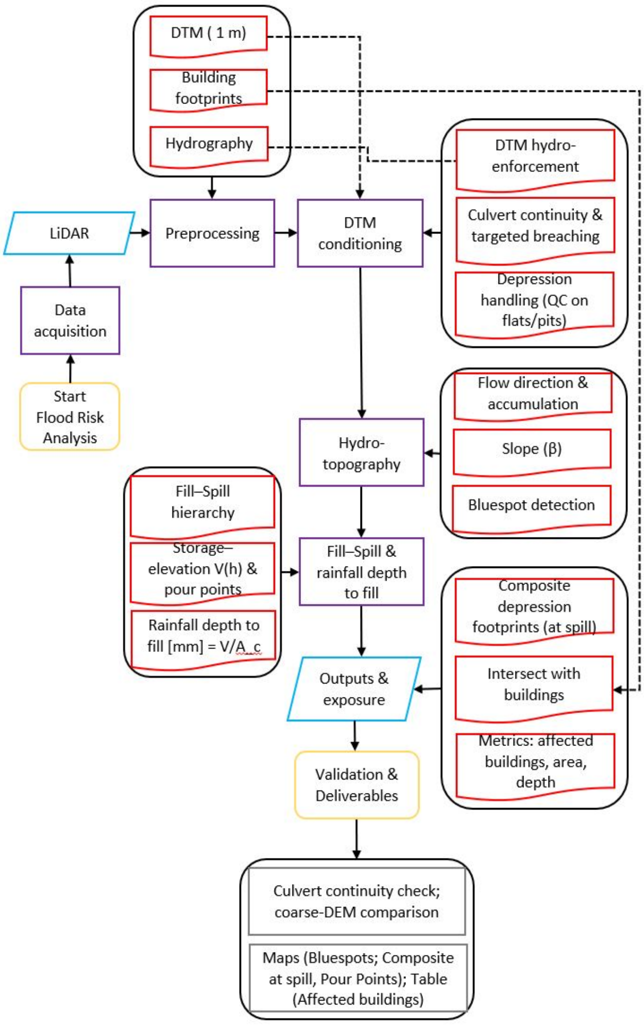

Figure 2. Methodological flowchart

A. *Inputs and pre-processing*

The workflow uses three inputs: the 1 m LiDAR-derived DTM, building footprints, and hydrography (rivers/culverts). Preprocessing comprised clipping to the study boundary, enforcing a common projection, and tiling for efficient raster processing. The 1 m DTM served as the sole elevation source for all derivatives and screening steps.

B. *DTM Hydrological Correction*

The 1 m DTM was hydrologically conditioned to restore downslope connectivity across roads/culverts and to remove artefactual pits before any routing or storage analysis [20]. On the raster grid (cell size = 1 m), local slope was computed for QA/QC with central differences:

$$z_x = \frac{z_{i+1,j} - z_{i-1,j}}{2 \cdot \text{cell size}} \tag{1}$$

$$z_y = \frac{z_{i,j+1} - z_{i,j-1}}{2 \cdot \text{cell size}} \tag{2}$$

$$\beta = \arctan\left(\sqrt{z_x^2 + z_y^2}\right) \tag{3}$$

Culvert continuity was imposed along mapped crossings Γ by writing a strictly monotone profile into the surface:

$$\tilde{z}_\Gamma(s) = z_{in} + \frac{z_{out} - z_{in}}{L} s \tag{4}$$

$$z(x) = \min\left[z(x), \tilde{z}_\Gamma(s(x)) - \varepsilon\right] \tag{5}$$

($\varepsilon > 0$ avoids flats), where embankments blocked lateral drainage, targeted breaching lowered a narrow channel-normal swath to connect upstream–downstream cells with a decreasing ramp. Spurious single-cell pits and flats caused by quantization were removed; true depressions were preserved for bluespot and fill–spill analysis. The conditioned surface z then supported flow direction/accumulation and the depression inventory used downstream.

C. *Hydrotopography: Flow Direction, Accumulation, Slope*

On the conditioned surface z, flow direction was computed with the D8 rule: for each cell i (cell size = 1 m), the downslope neighbor n is the one that maximizes the drop:

$$drop(i \to n) = \frac{z(i) - z(n)}{d_{in}} \tag{6}$$

with d_{in} = cell size for the four cardinal neighbors and $d_{in} = \sqrt{2}$ cell size for diagonals [21].

Given the resulting flow-pointer grid, flow accumulation $A(i)$ (in number of cells) satisfies the recursive conservation:

$$A(i) = 1 + \sum_{j \epsilon U(i)} A(j) \tag{7}$$

$$C(i) = (\text{cell size})^2 A(i)\left[\text{m}^2\right] \tag{8}$$

where $U(i)$ is the set of upslope neighbors whose flow direction points into i. The contributing area is then $C(i) = (\text{cell size})^2 A(i) \left[\text{m}^2\right]$. This provides the upslope convergence pattern needed for bluespot mapping and for extracting each depression's A_c. Slope β was retained from the gradient of z (as in Section III.B) and used alongside $A(i)$ to characterize preferential routing.

D. *Bluespot Detection and Attributes*

On the conditioned DTM z, bluespots were identified as maximal connected depressions whose interior cells are lower than their surrounding rim [2]. For each depression Ω, the pour point p_{out} is the lowest cell on its boundary; the corresponding spill elevation is $h = z(p_{out})$. The local depth field at spill is:

$$d(x) = \max\left\{0, h - z(x)\right\},\ x \in \Omega \tag{9}$$

and the storage volume at spill is the discrete integral on the 1 m grid

$$V(h) = \sum_{x \epsilon \Omega} d(x)(\text{cell size})^2,\ \text{cell size} = 1\ \text{m} \tag{10}$$

The contributing area A_c was extracted by delineating the upslope watershed of p_{out} on the flow-direction grid (Section III.C). Each bluespot polygon was attributed with

Digital Object Identifier 10.32754/JMT.2026.1.19

planimetric area, h, maximum depth d, $V(h)$, and A_c, providing the inputs for the rainfall-to-fill screening in Section III.F.

E. Fill–Spill Hierarchy and Storage–Elevation Curves

The bluespots were organised into a fill–spill hierarchy that captures how depressions fill, overflow through pour points, and merge downstream into composite storage units. Each depression Ω_k has a spill elevation h_k at its pour point and a directed edge to its downstream neighbor $\Omega_{k \to m}$. Processing the network in topological order yields a cascade in which upstream units fill → spill → merge into their receivers [13].

On the 1 m grid (cell size = 1 m), the storage–elevation relation for a depression (or composite) at water level h is:

$$V(h) = \sum_{x \in \Omega} \max\{0, h - z(x)\}(cell\, size)^2 \tag{11}$$

with the wetted area given by the derivative:

$$A_{wet}(h) = \frac{dV}{dh} \approx N_{\{z<h\}} (\text{cell size})^2 \tag{12}$$

where $N_{\{z<h\}}$ is the number of grid cells with $z(x) < h$. The spill threshold is reached when $h = h_k$; at that point, outflow is routed across the pour point to the mapped neighbor and polygons/attributes are merged to form a composite unit. Each (composite) unit retains h, max d, $V(h)$, and its upslope contributing area A_c, used for rainfall-to-fill screening in Section III.F.

F. Rainfall–Storage Coupling and Screening Rule

For each depression (or composite unit) the rainfall depth required to fill to spill is:

$$d_{fill}[mm] = \frac{V(h_{spill})}{A_c} \times 10^3 \tag{13}$$

where $V(h)$ is the storage volume at spill (m³) and A_c the contributing area (m²). Screening accounted for a local drainage-capacity threshold of 30 mm·h⁻¹. For a design hyetograph $R(t)$ [mm h⁻¹] over duration T,

$$D_{eff}[\text{mm}] = \int_0^T \max(0, R(t) - 30)\, dt \tag{14}$$

and a unit is flagged to spill when $D_{eff} \geq d_{fill}$. This event-based filling logic follows recent hierarchical filling–spilling formulations for pluvial screening [22].

G. Outputs and Building Exposure

At the spill threshold h, polygons of composite depression footprints act as inundation masks. Intersecting these masks with building footprints yields exposure metrics such as the count of affected buildings N_b, inundated footprint area a_b, and maximum within-footprint depth $d_b^{\max}$

$$N_b = \left|\{b : area(footprint_b \cap composite) > 0\}\right| \tag{15}$$

$$a_b = area(footprint_b \cap composite) \tag{16}$$

$$d_b^{max} = \max(h - z(x)), x \in (footprint_b \cap composite) \tag{17}$$

Results are aggregated at settlement level for reporting and mapping [23].

H. Visualisations, Checks, and Deliverables

To aid communication, 2D/3D water-level visualisations (+1 m, +2 m) were produced on the conditioned DTM, and a side-by-side view with a coarse DEM was used to illustrate the added value of LiDAR [24]. Connectivity at culverts and road crossings was verified to ensure continuous routing. For the summary tables, depth outliers greater than 5 m—attributable to seam/polygonisation or unit mismatches—were treated as artefacts and capped at 5 m for reporting only; mapped composites and exposure counts remain unchanged. Final deliverables comprise maps of bluespots, composite footprints at spill (with pour points), and a table of affected buildings intended for stakeholder use.

IV. Results and Discussion

The workflow outputs a hydrologically conditioned 1 m DTM, a bluespot inventory with spill thresholds and storage attributes, rainfall-to-fill screening (mm = V/A_c), and a building-level exposure layer. Results are reported from the initial risk layer through rainfall-based screening and communication views, using the figures already produced in the technical report.

A. Initial Flood-Susceptibility Layer (Bluespots and Exposed Buildings)

The baseline map combines the depression inventory ("bluespots") with building footprints to screen where structures lie within or immediately adjacent to potential ponding (Fig. 3). Bluespots cluster along the Argeșel corridor and around the tributary confluences near Hârtiești, Dealu, and Vulturești, reflecting local topographic controls on storage and overland flow. In the cartographic convention used here, buildings intersecting bluespots are highlighted (yellow) against the full building layer (red), making high-priority assets visually prominent for follow-up checks and mitigation planning.

Spatial patterns are consistent with field-intuitive expectations: ponding pockets concentrate in low relief near the main channel and along valley bottoms, while smaller hollows appear on hillslopes above Vulturești and in the Valea lui Topor/Mâzgana sectors. This arrangement underscores the role of local relief and road embankments in shaping storage and connectivity, and it frames subsequent analysis of spill thresholds $(\text{mm} = V/A_c)$.

Descriptive statistics from the same layer indicate that a non-trivial share of the building stock falls within or touches mapped depressions; the report summarises this as roughly ~5% of buildings across the study area, with up to 67 buildings identified as at heightened risk under severe rainfall scenarios.

 Digital Object Identifier 10.32754/JMT.2026.1.19

These counts provide a first-order prioritisation list for site inspection and local drainage improvements.

Figure 3. Baseline flood-susceptibility map: bluespots and buildings intersecting or adjacent to depressions in Hârtiești, Dealu, and Vulturești (Argeșel Basin)

To aid interpretation at settlement scale, the reference map also includes zoomed insets for the Valea lui Topor and Mâzgana tributaries, where direct building–bluespot contact is evident. These insets help localise specific assets and road segments for targeted measures (e.g., culvert maintenance, small conveyance works).

B. Descriptive Statistics and Exposure Counts

The bluespot inventory and the building overlay yield a concise picture of potential impact at settlement scale. Summary tables report, for each mapped depression, planimetric area, maximum depth, spill elevation, storage at spill $V(h\_\text{spill})$, and contributing area A_c ; a companion table lists buildings intersecting spill-onset composites, with inundated footprint area and depth indicators. Across Hârtiești, Dealu, and Vulturești, the tallies indicate that about five percent of the building stock lies within or touches depressions, with the largest concentrations aligned to floodplain pockets along the Argeșel corridor. These counts provide a practical prioritisation list for site checks (e.g., local drainage maintenance at culverts/road crossings) and for targeting small protective works.

At locality level, the distribution of affected assets mirrors the topographic setting: low-relief sectors near tributary confluences contribute most of the flagged buildings, while isolated exposures occur on hillslopes where small hollows coincide with construction. Because the indicators are computed at the spill threshold, they represent a conservative, reproducible screening baseline that is consistent across the basin; subsequent sections complement this view with rainfall-to-fill thresholds (Section IV.C) and communication views (+1 m/+2 m). Depth statistics reported in Tables I–II are capped at 5 m to minimise the influence of obvious artefacts; maps use the raw values.

Table I summarises the range of bluespot attributes at the spill threshold across the study area.

TABLE I. ATTRIBUTE RANGES FOR POTENTIAL FLOOD ZONES (BLUESPOTS) AT SPILL LEVEL (MAX DEPTH CAPPED AT 5 M)

	Min	Max (capped at 5 m)
Number of zones (polygons)	1	3531
Area (m²)	2.56	1935.36
Volume (m³)	0.0189	921.1512
Depth (m)	0.0009	≤ 5.00

Note: Depth values > 5 m were flagged as artefacts and capped at 5 m for tables only; maps and exposure counts remain unchanged.

Table II reports the range of building attributes for footprints intersecting spill-onset composites.

TABLE II. ATTRIBUTE RANGES FOR BUILDINGS INTERSECTING COMPOSITE SPILL FOOTPRINTS

	Min	Max
Buildings	1	67
Length (m)	12.8	224
Area (m²)	10.24	947.2

C. Rainfall-to-Fill Thresholds and Spill-onset Composites

Screening by rainfall depth to fill $(\text{mm} = V/A_c)$ ranks depressions by how quickly they reach spill under effective rainfall. Across the inventory (N = 75), values range from ~0 mm to ≈56 mm, with a mean of 5.14 mm and a standard deviation of 8.88 mm. The distribution is strongly right-skewed: ≈83% of units are ≤10 mm (0–5: 50; 5–10: 12), and ≈96% are ≤30 mm (10–15: 4; 15–20: 3; 20–25: 2; 25–30: 1). Only three depressions exceed 30 mm (30–35: 1; 35–40: 1; 55–60: 1, max ≈56 mm), indicating that most storage pockets would spill under modest totals.

Composite spill footprints colour-coded by rainfall-to-fill classes reveal where small amounts are sufficient to trigger overflow, especially along the Argeșel floodplain and at the Valea lui Topor/Mâzgana confluences. Warm classes (e.g., 30–50 mm) cluster near dense building fabric and road embankments, suggesting sensitivity to culvert performance and local blockage; cooler classes on shoulder slopes and terrace edges denote storage-dominated pockets that require larger totals to spill.

Operationally, the mm-to-fill threshold translates complex micro-topography into a site-specific action cue: footprints touching buildings in the 30–50 mm band mark priority spots for targeted maintenance actions (debris clearance at crossings, reopening blocked inlets, minor grading to restore drainage). Because thresholds derive directly from $V\left(h_{spill}\right)$ and A_c on the 1 m DTM, the ranking is reproducible across localities and can be re-run after targeted works to verify whether highlighted polygons shrink or cool.

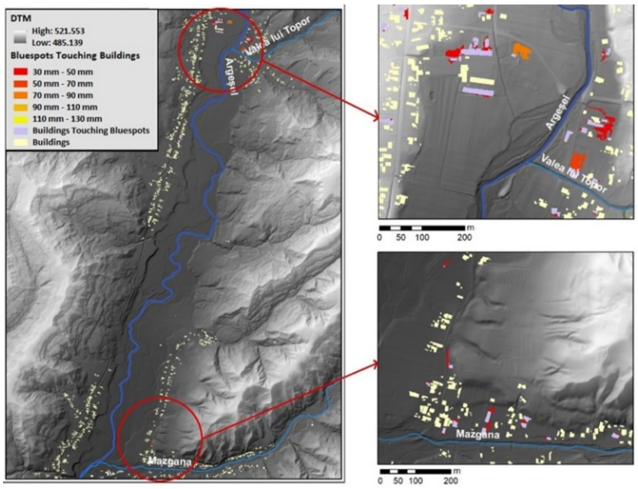

Figure 4. Rainfall-to-fill composites (mm) with buildings; insets: Valea lui Topor and Mâzgana

D. 2D Communication View: +1 m and +2 m Water Levels

A simple 2D water-level rise visualisation (+1 m, +2 m) on the conditioned DTM corroborates the bluespot patterns and gives non-specialists an intuitive sense of progressive encroachment near settlements. The map stacks two thresholds over an orthophoto backdrop +1 m in yellow and +2 m in blue, so viewers can immediately see how ponding expands from floodplain pockets toward building clusters along the Argeșel corridor and at the Valea lui Topor/Mâzgana confluences. This view is especially helpful for briefings and public communication because it requires no technical reading of storage curves or rainfall thresholds while remaining consistent with the terrain-driven analysis.

Interpretation follows the same logic as the screening layers: yellow footprints typically hug low-relief areas and road embankments; where these polygons touch or overlap buildings, they point to locations where modest rises in water level could produce nuisance flooding of parcels, access roads, or service yards. Blue areas show the plausible upper envelope under a larger rise, useful for contingency planning and for prioritising assets that would be affected in a second stage of encroachment. The 2D view complements, rather than replaces, mm-to-fill rankings by providing a visual narrative of how susceptibility escalates across the landscape.

Because the product is a level-rise depiction on the DTM (not a dynamic hydraulic simulation), interpretation should acknowledge common limitations noted in the technical report (e.g., it does not resolve building base elevations or within-channel hydraulics, and it generalises drainage performance). Used alongside the bluespot and rainfall-to-fill layers, it remains a powerful communication and triage tool for local maintenance and preparedness workflows.

E. Three-Dimensional Level-Rise Visualisations (+1 m, +2 m)

Oblique 3D visualisations on the conditioned 1 m DTM make the terrain–building interface tangible at settlement scale. At +1 m, shallow encroachment closely follows the low-relief pockets already mapped as bluespots, hugging road embankments and parcel edges along the Argeșel corridor. Around the Valea lui Topor and Mâzgana confluences, the perspective view clarifies how micro-topography and linear infrastructure can momentarily impound water against structures under modest rises, highlighting places where culvert condition is likely to be decisive.

Figure 5. 2D water-level rise visualisation on the 1 m DTM (+1 m = yellow; +2 m = blue) overlaid on the orthophoto; encroachment concentrates along the Argeșel corridor and at the Valea lui Topor/Mâzgana confluences

At +2 m, isolated pockets coalesce along valley bottoms and terrace breaks, sketching a plausible upper envelope for local contingency planning. Read together with the rainfall-to-fill ranking $(\mathrm{mm} = V/A_c)$, these renders offer a clear, non-technical narrative for stakeholders: where warm classes touch buildings, +1 m scenes show the first tier of concern; where composites span multiple parcels, +2 m scenes illustrate how exposure scales if water levels continue to rise. The 3D views are intended for briefings and community engagement and complement rather than replace the analytical screening layers.

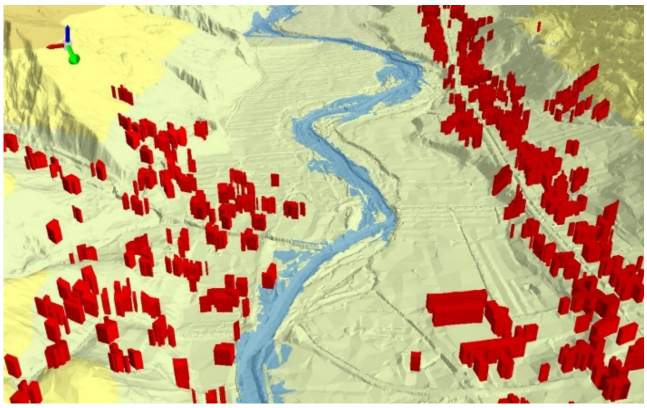

Figure 6. 3D water-level view on the 1 m DTM (+1 m), with detail at the Valea lui Topor and Mâzgana hotspots

 Digital Object Identifier 10.32754/JMT.2026.1.19

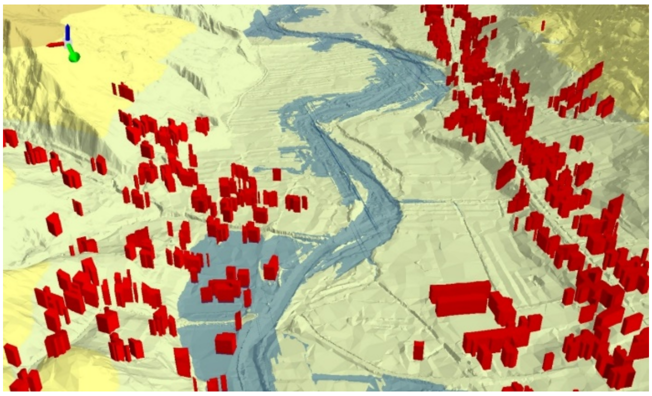

Figure 7. 3D water-level view on the 1 m DTM (+2 m), showing coalescence of pockets along valley bottoms and embankments

V. Limitations and Future Work

The screening rests on a static, hydrologically conditioned 1 m DTM and does not simulate fully resolved hydrodynamics in channels or floodplains. Building base elevations (floor levels) are unavailable, so exposure is assessed at footprint level, which may over- or understate actual damage potential. The rainfall-to-fill metric $(\text{mm} = V(h_{spill})/A_c)$ assumes uniform, effective rainfall and a fixed local drainage-capacity threshold (30 mm·h^{-1}); temporal variability in intensity, infiltration, and soil storage is not explicitly represented. After spill, overflow is routed via pour points into composite units defined at the spill threshold, yet the time-dependent cascading of volumes is not modelled. As with any terrain-first approach, LiDAR artefacts (classification errors, seam effects) and incomplete culvert inventories can influence local results; obvious depth outliers (> 5 m) were treated as artefacts and capped in summary tables, while maps retain raw values. Lastly, the coarse-to-fine comparison illustrates LiDAR benefits qualitatively, but systematic validation against observed flood extents or high-water marks was beyond scope.

Several targeted enhancements would strengthen operational value. Floor-level surveys (or photogrammetric extraction where feasible) would enable building-specific impact thresholds. Incorporating dynamic losses (e.g., Green–Ampt or SCS-CN) and event hyetographs would refine the translation from rainfall to effective filling. Coupling with 1D/2D hydraulic models on selected reaches would quantify within-channel capacity, backwater, and floodplain conveyance while retaining the terrain-based triage provided here. A structured culvert inventory (span, invert, blockage likelihood) could be integrated to test maintenance scenarios and their effect on spill-onset composites. Calibrating and benchmarking the workflow against documented events in Hârtiești and Vulturești, then repeating the analysis after small-scale interventions, would turn the mm-to-fill layers into a simple monitoring dashboard for local preparedness.

VI. Conclusions

A LiDAR-driven, GIS-centric screening was assembled for the Argeșel Basin to identify terrain-controlled flood susceptibility at building scale. A hydrologically conditioned 1 m DTM underpinned the analysis: depressions (“bluespots”) were mapped, organised into a fill–spill hierarchy, and attributed with storage–elevation relations and contributing area. Translating storage and upslope area into a rainfall-to-fill threshold $(\text{mm} = V(h_{spill})/A_c)$ produced an interpretable, location-specific indicator that ranks where overflow would occur under effective rainfall. Intersecting spill-onset composites with building footprints yielded an exposure layer suitable for prioritising site checks and small maintenance works.

Results show coherent patterns: susceptibility clusters along the Argeșel corridor and at the Valea lui Topor and Mâzgana confluences; many depressions reach spill under modest effective rainfall, and dozens of buildings fall within or touch spill-onset composites, with concentrations in Hârtiești and Vulturești. The approach adds operational value by converting complex micro-topography into actionable thresholds, while the +1 m/+2 m level-rise views provide a clear communication aid for non-specialists. Compared with coarser DEMs, the LiDAR surface improves drainage connectivity and the credibility of mapped storage, supporting more focused mitigation planning.

The workflow is reproducible, lightweight, and transferable to nearby small catchments. In practice, the maps can guide priority maintenance works - culvert cleaning, reopening blocked inlets, minor grading to restore connectivity—starting with warm-class composites that touch buildings. Re-running the screening after interventions can document change and establish a simple monitoring loop for local preparedness, while targeted hydraulic modelling on selected reaches can complement the terrain-first triage where greater detail is required.

References

[1] R. Barnes, C. Lehman, & D. Mulla, "Priority-Flood: An optimal depression-filling and watershed-labeling algorithm for digital elevation models", *Computers & Geosciences*, vol. 62, pp. 117–127, Jan. 2014. doi:10.1016/j.cageo.2013.04.024

[2] T. Balstrøm, & D. Crawford, "Arc-Malstrøm: A 1D hydrologic screening method for stormwater assessments based on geometric networks", *Computers & Geosciences*, vol. 116, pp. 64–73, Jul. 2016. doi:10.1016/j.cageo.2018.04.010

[3] N. A. Muhadi, A. F. Abdullah, S. K. Bejo, M. R. Mahadi, & A. Mijic, "The use of LiDAR-derived DEM in flood applications: A review", *Remote Sensing*, vol. 12, no. 14, 2308, Jul. 2020. doi:10.3390/rs12142308

[4] J. B. Lindsay, "Efficient hybrid breaching-filling sink removal methods for flow path enforcement in digital elevation models", *Hydrological Processes*, vol. 30, no. 6, 2016, pp. 846–857. doi:10.1002/hyp.10648

[5] C. A. Kelleher, & L. E. McPhillips, "Exploring the application of topographic indices in urban areas as indicators of pluvial flooding locations", *Hydrological Processes*, vol. 34, no. 3, pp. 780–794, Oct. 2019. doi:10.1002/hyp.13628

[6] E. Huțanu, A. Mihu-Pintilie, A. Urzica, L.-E. Paveluc, C.-C. Stoleriu, & A. Grozavu, "Using 1D HEC-RAS modeling and LiDAR data to improve flood hazard maps accuracy: A case study from Jijia Floodplain (NE Romania)" *Water*, vol. 12, no. 6, 1624, Jun. 2020. doi:10.3390/w12061624

[7] C.-C. Stoleriu, A. Urzica, A. Mihu-Pintilie, "Improving flood risk map accuracy using high-density LiDAR data and the HEC-RAS river analysis system: A case study from north-eastern Romania", *Journal of Flood Risk Management*, 13(S1), 2020, e12572. doi:10.1111/jfr3.12572

[8] H. Wei, G. Zhou, S. Fu, "Efficient Priority-Flood depression filling in raster digital elevation models", *International Journal of Digital Earth*, vol. 12, no. 4, pp. 415–427, 2019. doi:10.1080/17538947.2018.1429503

[9] K. Woodrow, J. B. Lindsay, A. A. Berg, "Evaluating DEM conditioning techniques, elevation source data, and grid resolution for field-scale hydrological parameter extraction", *Journal of Hydrology*, 540, pp. 1022–1029, 2016. doi:10.1016/j.jhydrol.2016.07.018

[10] S. Saksena, V. Merwade, "Incorporating the effect of DEM resolution and accuracy for improved flood inundation mapping", *Journal of Hydrology*, vol. 530, pp. 180–194, Nov. 2015. doi:10.1016/j.jhydrol.2015.09.069

[11] F. McClean, R. Dawson, C. Kilsby, "Implications of Using Global Digital Elevation Models for Flood Risk Analysis in Cities", *Water Resources Research*, vol. 56, no. 10, Oct. 202, e2020WR028241. doi:10.1029/2020WR028241

[12] L. Hawker, J. Rougier, J. Neal, P. Bates, "Perspectives on Digital Elevation Model (DEM) Simulation for Flood Modeling in the Absence of a High-Accuracy Open DEM", *Frontiers in Earth Science*, vol. 6, 233, Dec. 2018. doi:10.3389/feart.2018.00233

[13] R. Barnes, K. L. Callaghan, A. D. Wickert, "Computing water flow through complex landscapes – Part 3: Fill–Spill–Merge: Flow routing in depression hierarchies", *Earth Surface Dynamics*, vol. 9, no. 1, pp. 105–121, Mar. 2021. doi:10.5194/esurf-9-105-2021

[14] P. D. Bates, N. Quinn, C. Sampson, A. Smith, O. Wing, J. Sosa, J. Savage, G. Olcese, J. Neal, G. Schumann, and A. Domeneghetti, "Combined Modeling of US Fluvial, Pluvial, and Coastal Flood Hazard Under Current and Future Climates", *Water Resources Research*, vol. 57, no. 2, 2021, e2020WR028673. doi:10.1029/2020WR028673

[15] Q. Wu, C. R. Lane, L. Wang, M. K. Vanderhoof, J. R. Christensen, H. Liu, "Efficient Delineation of Nested Depression Hierarchy in Digital Elevation Models for Hydrological Analysis Using Level-Set Method", *Journal of the American Water Resources Association*, vol. 55, no. 2, pp. 354–368, Apr. 2019. doi:10.1111/1752-1688.12689

[16] S. Boengiu, A. Vlăduț, E. Marinescu, "Conditions of gully development within piedmont areas with examples from the western part of the Getic Piedmont, Romania", *Journal of Environmental Biology*, vol. 33(2 Suppl), pp. 407–415, Apr. 2012.

[17] C. Popescu, A. Bărbulescu, "Floods Simulation on the Vedea River (Romania) Using Hydraulic Modeling and GIS Software: A Case Study", *Water*, vol. 15, no. 3, 2023, 483. doi:10.3390/w15030483

[18] M. J. Adler, R. Amafteesei, R. Mic, V. A. Stănescu, "The flooded areas risk. Argeș basin application", in *Proc. of the AMHY-FRIEND International Workshop on Hydrological Extremes*, Cosenza, Italy, May 3–4, 2006, pp. 81-90.

[19] RIEGL Laser Measurement Systems GmbH. (2012). LMS-Q680i Airborne Laser Scanner: Technical datasheet. Horn, Austria: RIEGL

[20] A.-L. Jiang, K. Hsu, B. F. Sanders, and S. Sorooshian, "Topographic hydro-conditioning to resolve surface depression storage and ponding in a fully distributed hydrologic model", *Advances in Water Resources*, vol. 176, 2023, 104449. doi:10.1016/j.advwatres.2023.104449

[21] J. F. O'Callaghan, D. M. Mark, "The extraction of drainage networks from digital elevation data", *Computer Vision, Graphics, and Image Processing*, vol. 28, no. 3, pp. 323–344, Dec. 1984. doi:10.1016/S0734-189X(84)80011-0

[22] C. Samela, S. Persiano, S. Bagli, V. Luzzi, et al., Safer_RAIN: A DEM-Based Hierarchical Filling-&-Spilling Algorithm for Pluvial Flood Hazard Assessment and Mapping across Large Urban Areas, *Water*, vol. 12, no. 6, 1514, May 2020. doi:10.3390/w12061514

[23] R. Bertsch, V. Glenis, C. Kilsby, "Building level flood exposure analysis using a hydrodynamic model", *Environmental Modelling & Software*, Vol. 156, Oct. 2022, 105490. doi:10.1016/j.envsoft.2022.105490

[24] S. E. Percival, M. Gaterell, D. Hutchinson, "Effective flood risk visualisation", *Natural Hazards*, vol. 104, pp. 375–396, Jul. 2020. doi:10.1007/s11069-020-04173-8.